

1 **Use of an Uncrewed Aerial System to Investigate Aerosol Direct and Indirect Radiative**
2 **Forcing Effects in the Marine Atmosphere**

3
4 Patricia K. Quinn¹, Timothy S. Bates², Derek J. Coffman¹, James E. Johnson², and Lucia M.
5 Upchurch²

6
7 ¹NOAA Pacific Marine Environmental Laboratory, Seattle, WA 98115, USA

8 ²University of Washington Cooperative Institute for Climate, Ocean, and Ecosystem Studies,
9 Seattle, WA 98105, USA

10 *Correspondence to:* Patricia K. Quinn (patricia.k.quinn@noaa.gov)

11 **Abstract**

12
13 An uncrewed aerial system (UAS) has been developed for observations of aerosol and cloud properties relevant to
14 aerosol direct and indirect forcing in the marine atmosphere. The UAS is a hybrid quadrotor – fixed wing aircraft
15 designed for launch and recovery from a confined space such as a ship deck. Two payloads, Clear Sky and Cloudy
16 Sky, house instrumentation required to characterize aerosol radiative forcing effects. The observing platform (UAS
17 plus payloads) has been deployed from a ship and from a coastal site for observations in the marine atmosphere. We
18 describe here the details of the UAS, the payloads, and first observations from the *TowBoatUS Richard L. Becker*
19 (March 2022) and from the Tillamook UAS Test Range (August 2022). [The development of this UAS technology](#)
20 [for flights from ships and coastal locations is expected to greatly increase observations of aerosol radiative effects in](#)
21 [the marine boundary layer over both temporal and spatial scales.](#)

22
23 **1. Introduction**

24 Atmospheric aerosol particles affect the Earth’s radiation budget directly by scattering and absorbing incoming solar
25 radiation and indirectly by taking up water and forming cloud droplets. Chemical composition of the particles
26 determines, in part, whether they scatter incoming solar radiation back to space which leads to cooling at the Earth’s
27 surface or absorb radiation and warm layers within the atmosphere (e.g., Li et al., 2022). The amount of heating
28 depends on the vertical distribution of the absorbing aerosol layer, whether it is located above or below clouds, and
29 the albedo of the surface (Takemura et al., 2002; Haywood and Ramaswamy, 1998). Whether particles act as cloud
30 condensation nuclei (CCN) and nucleate cloud droplets depends on their size and chemical composition (Lohmann
31 and Feichter, 2005). If the particles are large enough and contain sufficient soluble material, an increase in particle
32 number can lead to an increase in cloud droplet number concentration and cloud albedo thereby leading to a cooling
33 at the Earth’s surface. The degree to which aerosol direct and indirect forcing are cooling the planet and offsetting
34 warming by greenhouse gases is highly uncertain. According to the International Panel on Climate Change (IPCC),
35 aerosols contribute the largest uncertainty in quantifying present-day climate change (IPCC, 2021).

36 Vertical profiles of aerosol and cloud properties are required to improve models and decrease uncertainties,
37 particularly over oceans due to the susceptibility of marine clouds to small changes in aerosol concentrations

38 (Rosenfeld et al., 2019). While satellite observations have the advantage of providing global coverage, *in situ*
39 observations have the highest level of accuracy available to constrain radiative forcing and reduce uncertainties in
40 forcing estimates (Li et al., 2022). Crewed aircraft have been used for the past several decades to characterize
41 horizontal and vertical distributions of aerosol and cloud properties relevant to radiative forcing (e.g., Russell et al.,
42 1999; Yoon and Kim, 2006; Zhang et al., 2017). These measurements come at a relatively high cost and require
43 extensive logistical coordination.

44
45 Uncrewed aerial systems, or UAS, have the advantage of lower costs and flexibility and frequency of flights
46 compared to crewed aircraft. In addition, they offer higher spatial resolution due to their relatively slow flight speed.
47 UAS have been used since the mid-2000s to measure aerosol and cloud properties relevant to radiative forcing
48 including particle number concentration and size distribution, light absorption, aerosol optical depth, and cloud drop
49 number and effective radius. These measurements have been made with vertical-take-off-and landing (VTOL) UAS,
50 either quadcopters (Brady et al., 2016) or hexacopters (e.g., Chilinski et al., 2016; Aurell et al., 2017), or fixed wing
51 UAS (Corrigan et al., 2008; Bates et al., 2013). The VTOL UAS that have been used have the advantage of not
52 needing a catapult or runway to be launched and recovered but typically have short endurance (< 30 min) and a
53 limited altitude ceiling (~1 km). The fixed wing aircraft that have been used require a launch and recovery apparatus
54 or a runway but have the advantage of longer duration (hours) and can reach high altitudes of 3 km or more. While
55 some VTOLs used can carry relatively heavy payloads (6 kg or more), they can only do so for ~ 15 min while some
56 of the fixed wing UAS can carry heavy payloads for hours.

57
58 We report here on measurements of aerosol and cloud properties using a hybrid quadrotor – fixed wing UAS, the
59 Fixed Wing VTOL Rotator or FVR-55, developed by L3Harris Latitude Engineering. The hybrid quadrotor – fixed
60 wing concept combines the advantages of fixed wing flight with the ability to take-off and land vertically thus
61 eliminating the need for a runway and allowing for launch and recovery from ships and other confined spaces. The
62 FVR-55 has an endurance of more than 4 hours, a height ceiling of at least 3 km, and can carry a 6 kg payload.
63 NOAA PMEL has developed two UAS payloads -- one for the measurement of aerosol properties relevant to direct
64 radiative forcing (Clear Sky) and one for the measurement of aerosol and cloud properties relevant to indirect
65 forcing (Cloudy Sky). The FVR-55 and instrumentation in the two payloads are described herein along with the
66 results of its first shipboard and coastal flights.

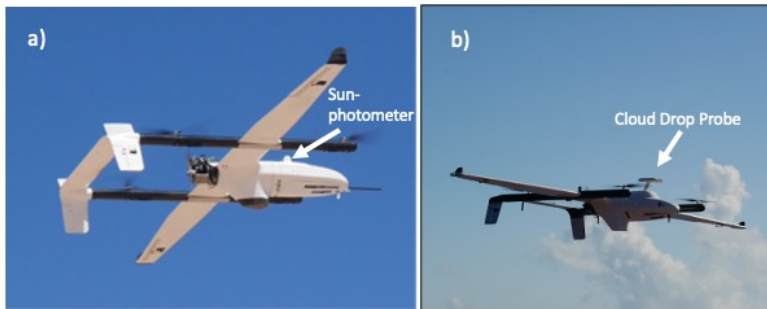
67 68 **2. Methods**

69 70 **2.1. FVR-55**

71
72 The FVR-55, a class II medium endurance UAS, was developed by Latitude Engineering (since acquired by
73 L3Harris) with support from NOAA Phase I and II SBIRs (Small Business Innovation Research awards) (see Figure
74 1). The focus of the SBIR was a UAS able to carry a 5.5 kg payload, have a flight ceiling of up to 3 km, an

75 endurance of 3 hrs or more, and a pusher engine. The hybrid quadrotor – fixed wing design of the FVR-55 combines
76 the high-power density of electric motors and propellers with the high-energy density of a piston engine and liquid
77 fuel. The electric-quadrotor system is used during launch and recovery (high power, short endurance) and the gas
78 engine is used for fixed wing flight (low power, long endurance). The aircraft has an empty weight of 20 kg and a
79 maximum take-off weight of 29.5 kg. It cruises at 25 m s⁻¹. A Cloud Cap Piccolo autopilot flight controller is used
80 for autonomous flight. In the case of a lost link, the avionics guides the UAS to a predetermined return to base
81 location and, if communication is not re-established, to land at an established target. A mobile ground control station
82 (Windows tablet or Laptop with Datalink) provides ground command and control. A differential GPS (dGPS)
83 system is used for computing the aircraft’s heading to circumvent the challenges created by the hull of a ship
84 distorting the Earth’s magnetic field. The fuselage of the FVR-55 was designed for a maximum spacing of the two
85 dGPS antennas to increase the accuracy of the computed heading. VTOL motors and propellers provide enough
86 overall power for the FVR-55 to handle turbulence created by relative wind blowing over the superstructure of a
87 ship. A “pusher engine” is used to minimize contamination of sample air in flight by ~~exhausting the engine aft while~~
88 ~~the UAS flies forward. When the flight track includes circles or spirals engine contamination can occur but is readily~~
89 ~~identifiable by short-lived increases in particle number concentration. We removed all data during these~~
90 ~~contaminated periods.~~ Individual payloads are integrated into a nose cone to allow for easy swapping of payloads
91 between flights. Payloads are powered at 12VDC from the plane with 200 W of power available.

92
93 Figure 1. FVR-55 with a) Clear Sky and b) Cloudy Sky payloads onboard.



94
95

Deleted: engine

Formatted: Font: (Default) Times New Roman, 10 pt

Formatted: Font: (Default) Times New Roman, 10 pt

Formatted: Font: (Default) Times New Roman, 10 pt

Deleted:

98 Table 1. Specifications of the FVR-55 UAS.
99

Cruise speed	25 m s ⁻¹
Weight with no payload or fuel	20 kg
Maximum take-off weight	29.5 kg
Endurance at maximum take-off weight including a 6.0 kg payload	4.5 hrs
Altitude ceiling	3,050 m
VTOL landing on land or ship	6 m x 6 m recover area
Size	4 m x 2.1 m x 0.3 m

100
101
102
103
104
105
106
107
108
109
110
111
112
113
114
115
116
117
118
119
120
121
122
123
124
125

2.2. Payloads

2.2.1. Inlet, sample air flow, and data acquisition

An isokinetic inlet is mounted on the nose cone of the FVR-55 to bring sample air into the payload under vacuum (See Figure 2). No changes in particle number concentration coinciding with the UAS transitioning from large spirals (1 to 2 km) to level leg flights were observed, indicating the performance of the isokinetic inlet was not impacted by a spiral flight pattern. Since particle number concentrations are dominated by the submicron size range this metric does not rule out effects in supermicron size ranges. In addition, the slow air speed of the UAS (25 m sec⁻¹) is expected to decrease impacts of the flight pattern on transmission of submicron particle through the inlet into the payload. Wind tunnel tests are planned for the determination of the particle passing efficiency as a function of air speed and particle size.

Sample air first encounters an inline water trap where water droplets are removed through impaction. The water trap has two outlets -- one outlet is for the sample line, which is under vacuum. The larger outlet exhausts condensate through a drain line that also allows excess ram air to passively exit the sampling system. Individual instruments sub-sample off of the sample inlet. For the Clear Sky payload, a perma pure drier is located downstream of the water trap and upstream of all instruments except the filter sampler (Figure 2a). For the Cloudy Sky payload, a perma pure drier is located downstream of the water trap and upstream of the mSEMS (Figure 2b). A restricting orifice and filter on the inlet of the perma pure sheath air combined with a vacuum on the outlet of the sheath air was used to remove moisture from the sample stream. Instruments are cooled in flight by air flow through vent shafts cut into the nose cone frame. More details about the instruments in each payload are provided in Sections 2.2.2. (Clear Sky) and 2.2.3. (Cloudy Sky).

Deleted:Page Break.....

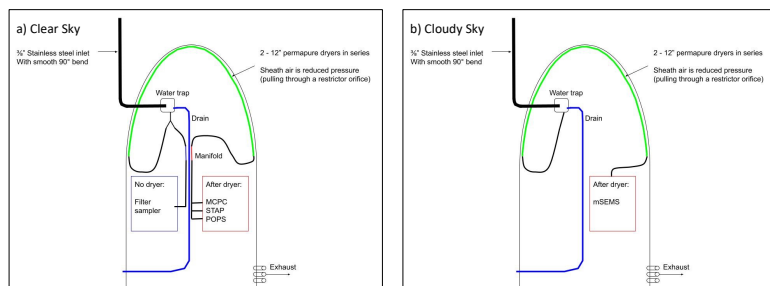
Deleted: . The inlet has an inline water trap with two outlets. O...

Deleted: any condensation to the atmosphere

Deleted: A

Deleted: instruments in the nose cone.

132 **Figure 2. Flow diagrams for a) Clear Sky and b) Cloudy Sky payloads.**



133
134
135 The data acquisition (DAQ) systems for the two payloads use different hardware and software but have the same
136 functionality. The Clear Sky payload DAQ is an Arduino based system that uses Labview software to collect data
137 and control the sensors. The Cloudy Sky payload uses a Raspberry PI running Python software to do the same. Both
138 DAQ systems collect and save data locally (on the aircraft) and also send data back to a ground station via a Silvus
139 radio link in near real-time. This communication link allows for command and control of the sensors during flight as
140 well as the ability to save a second copy of the data on the ground.

141
142 **2.2.2. Clear Sky Payload**

143
144 The Clear Sky Payload was designed to measure aerosol properties required for quantification of aerosol direct
145 radiative effects. All of the initial instruments in the payload were built by Brechtel Manufacturing Inc. (BMI,
146 Haywood, CA; ACCESS Model 9400) under a NOAA SBIR. The payload was first flown on a MANTA C1 UAS
147 from Ny-Ålesund, Svalbard, Norway in 2011 (Bates et al., 2013). The instruments included a mixing condensation
148 particle counter (MCPC) for measuring total particle number, or condensation nuclei (CN) concentration; a three-
149 wavelength Single Channel Tricolor Absorption Photometer (STAP) for measuring the aerosol light absorption
150 coefficient; and a multi-channel filter sampler for the collection of aerosol samples for post-flight chemical analysis.
151 Two instruments were added to the payload in 2014 including a Printed Optical Particle Spectrometer (POPS) for
152 the measurement of particle number size distribution (0.14 to 3 μm) (Telg et al., 2017) and a Mini Scanning Aerosol
153 Solar Photometer (mini-SASP) for the measurement of sun and sky radiance (Murphy et al., 2016). The payload also
154 includes Rotronic HC2-S3 and Innovative Sensor Technology (IST) HYT271 temperature and humidity sensors.
155 The updated version of the Clear Sky Payload was flown during a second campaign from Ny-Ålesund in 2015 (Telg
156 et al., 2017). A perma pure drier is plumbed into the sample line to provide dried air to the MCPC, STAP, and
157 POPS. The RH of the sampled air downstream of the drier was $34 \pm 1.6\%$, or $\sim 8\%$ lower than ambient RH, for
158 results reported here from a high-altitude flight off the coast of Oregon in August 2022. The Clear Sky Payload plus
159 the FVR-55 nose cone weighs 6 kg. The mini-SASP mounted on top of the FVR-55 nose cone is shown in Figure
160 1a. Table 2 lists the instruments in the Clear Sky Payload that were integrated into the FVR-55 nose cone. [Sampling](#)

Formatted: Font: Bold, Italic

Deleted: ¶

Deleted: 1

163 rates were 1 sec for all real time instruments while filter samples were collected over a period of minutes to hours.
 164 Further details on each instrument are provided below. Comparisons between Clear Sky and bench top instruments
 165 are presented in Sect. 3.

167 Table 2. Measured parameters and instrumentation in the Clear Sky Payload.

Clear Sky Payload Instrumentation			
Measured Parameter	Derivable Parameter(s)	Instrument	Uncertainty
Total particle number concentration, > 0.005 μm		Brechtel Mixing Condensation Particle Counter (MCPC)	$\pm 8\%^a$
Particle number size distribution, 0.14 to 3 μm	Scattering coefficient, asymmetry parameter, Ångstrom exponent ^b	Portable Optical Particle Spectrometer (POPS)	$\pm 10\%$ particle concentration accuracy
Aerosol light absorption coefficient (dry) (450, 525, and 624 nm)	Absorption aerosol optical depth (AOD _{abs}) Single scattering albedo when paired with scattering coefficient derived from the measured number size distribution	Brechtel Single Channel Tricolor Absorption Photometer (STAP)	$\pm 33\%$ at 1.0 Mm^{-1} , ^c
Sun and sky radiance (460.3, 550.4, 671.2, and 860.7 nm)	Aerosol optical depth (AOD)	Mini Scanning Aerosol Solar Photometer (mini-SASP)	0.01 detection limit (AOD)
Chemical composition (Na^+ , NH_4^+ , K^+ , Mg^{2+} , Ca^{2+} , Cl^- , NO_3^- , Br^- , SO_4^{2-})		Brechtel Multi-Channel Chemical Sampler	$\pm 5\%^d$ $\pm 8.5\%^e$
T		Rotronic HC2-S3 IST HYT271	$\pm 0.1^\circ\text{C}$ (<15 s) ^f $\pm 0.2^\circ\text{C}$ (<15 s) ^f
RH		Rotronic HC2-S3 IST HYT271	$\pm 0.8\%$ (<5 s) ^f $\pm 1.8\%$ (<4 s) ^f

168 ^aCoincidence corrected concentration uncertainty at 10,000 cm^{-3}

169 ^bUsing Mie theory

170 ^cBates et al. (2013)

171 ^dSample flow accuracy (uncertainty due to Chemical Sampler only)

172 ^eOverall uncertainty for the measurement of inorganic ions

173 ^fTime response

174
 175 The MCPC (modified BMI Model 1710) has a 0.18 s response time, grows particles in a butanol-saturated flow, and
 176 counts particles larger than 5 nm in diameter. Modifications to the butanol handling components of the commercial
 177 Model 1710 were implemented to address the high vibration environment of the UAS (Bates et al., 2013). The
 178 MCPC has a $\pm 8\%$ coincidence corrected uncertainty for a particle concentration of 10,000 cm^{-3} .

179
 180 The STAP provides real-time measurement of the aerosol light absorption coefficient at 450, 525, and 624 nm. Light
 181 is transmitted from an LED source through a sample and a reference filter. The filter transmission is the ratio of the
 182 signals from the two filters. The light absorption coefficient is proportional to the rate of decrease of light
 183 transmittance divided by the flow rate of air through the filter (Bond et al., 1999). The raw data are averaged into 60

Formatted: Line spacing: 1.5 lines

Deleted: ¶

186 sec values for the calculation of the rate of decrease of light transmittance. The minimum detectable level, MDL,
187 defined as the peak-to-peak noise with the instrument running particle free air, is 0.2 Mm^{-1} . Errors in the STAP
188 measurement include noise in the transmission value, uncertainty in the measured flow rate, and uncertainty in the
189 measured filter spot area (Anderson et al., 1999). A quadrature sum of these errors yields a relative uncertainty of \pm
190 33% at 1.0 Mm^{-1} . In addition, light scattering by particles collected on the sample filter can lead to an
191 overestimation of absorption values by $\sim 2\%$ of the observed scattering coefficient (Bond et al., 1999). A correction
192 for scattering was not performed on the data collected in August 2022. The temperature and relative humidity of the
193 sample air flow drawn into the STAP was $12 \pm 1.6^\circ\text{C}$ and $34 \pm 1.6\%$, respectively, for conditions encountered off of
194 the coast of Oregon in August 2022.

195
196 The Brechtel Multi-Channel Chemical Sampler has eight filter holders (13 mm diameter) and a magnetically-driven
197 rotary valve manifold that distributes the vacuum from a central pump to each of the sampling channels. A remote
198 serial command is used to move the rotary valve to a new sampling channel in flight. The sample flow rate is 2.5 L
199 min^{-1} which is measured by the pressure drop through a laminar flow element. One of the eight channels can be used
200 to maintain flow when a filter sample is not being collected. 13 mm Millipore Fluoropore 1.0 μm PTFE membrane
201 filters were used for sample collection. For the measurements reported here, filters were extracted post-flight in a
202 17% methanol/water solution for analysis by ion chromatography (IC). The volume of liquid used to extract the
203 filters was minimized to 1 mL to increase the sensitivity of the method. Filters were sonicated for 30 min. The filter
204 extract was injected into a Metrohm 940 Professional IC Vario with 889 IC Sample Center autosamplers and
205 analyzed for inorganic cations (Na^+ , NH_4^+ , K^+ , Ca^{2+} , Mg^{2+}) and anions (Cl^- , NO_3^- , SO_4^{2-}). A Metrosep C6 - 100/4.0
206 column, 2 mMol HNO_3 eluent, and a flow rate 0.9 ml min^{-1} were used for the cation analysis. Metrosep A Supp 5 -
207 250/4.0 and Phenomenex Star Ion A300- 100/4.6mm columns in serial, a 1 mMol NaHCO_3 and 5 mMol Na_2CO_3
208 eluant, and a flow rate of 0.7 ml min^{-1} were used for the anion analysis. Sources of uncertainty in the chemical
209 analysis include air volume sampled ($\pm 5\%$), the extract liquid volume ($\pm 3.5\%$), 2 times the standard deviation of
210 the blank, and precision/calibration of the method ($\pm 5\%$). Total average overall uncertainty was $\pm 8.5\%$. Only ion
211 concentrations above 2 times the standard deviation of the filter blank are reported here.

212
213 Particle number size distributions from 0.14 to $3.0 \mu\text{m}$ in diameter were measured with a POPS (Telg et al., 2017).
214 The POPS detects and sizes single particles based on the dependence of the scattering intensity on particle size. A
215 405 nm laser diode is used as a light source. The light scattering signal is collected at scattering angles between 38°
216 and 142° (Gao et al., 2016). As for the MCPC and the STAP, the temperature and RH of the sample air drawn into
217 the POPS was $12 \pm 1.6^\circ\text{C}$ and $34 \pm 1.6\%$, respectively, for conditions encountered off of the coast of Oregon in
218 August 2022. Uncertainty for the POPs is $\sim 10\%$ of the total particle concentration.

219
220 Sun and sky radiance were measured with a miniSASP at wavelengths of 460.3, 550.4, 671.2, and 860.7 nm
221 (Murphy et al., 2016). Four independent telescopes, each with a unique interference filter, are housed in a single
222 aluminium block. A heater is integrated with a temperature controller to minimize condensation and keep the

223 photodiodes at an approximately constant temperature. The miniSASP scans the sky at the elevation angle of the
224 sun. A full azimuth revolution is made in about 30 s and measurements are made every 30 ms. Sun angle is
225 corrected for the tilt of the UAS. Each revolution of the miniSASP's telescopes results in a distinct peak
226 corresponding to the intensity of direct sun light. The aerosol optical depth of an atmospheric layer on the slant path
227 is the difference between the sun signal and Rayleigh scattering. Flight data from Svalbard in 2015 show a detection
228 limit better than 0.01 in AOD for a vertical profile through the bottom few kilometers of the atmosphere.

229

230 2.2.3. Cloudy Sky Payload

231

232 The Cloudy Sky payload was designed to characterize the relationship between cloud drop number concentration
233 and particle number concentration and size below, within, and above cloud. The Cloudy Sky payload has a Brechtel
234 miniature Scanning Electrical Mobility Sizer (mSEMS) for the measurement of particle number size distribution
235 (0.01 to 0.3 μm) and total particle number concentration. A perma pure drier is plumbed into the sample line to
236 provide dried air to the mSEMS. The RH of the sheath air was measured during operation. The RH of the dried
237 sample air depended on ambient conditions but ranged from 35 to 45% for the flights from Tillamook. Operating
238 conditions for the mSEMS included a sheath flow rate of 2.5 lpm, sample flow rate of 0.36 lpm, and a size scan of
239 30 bins at 1 sec per bin resulting in a sampling rate of 30 sec for each size distribution.

240

241 A miniature and light weight Cloud Drop Probe (DMT, CDP-2) is used to measure cloud droplet number
242 concentration and size distribution between 2 and 50 μm . The payload also has Rotronic HC2-S3 and IST HYT271
243 temperature and humidity sensors. Cloudy Sky instrumentation and specifications are listed in Table 3. The Cloudy
244 Sky payload was integrated into an FVR-55 nose cone in March 2021 at the L3Harris facility in Tucson, Arizona.
245 The payload then flew three flights onboard the FVR-55 at the Florence Military Range up to an altitude of 2.6 km.
246 The cloud droplet probe mounted on top of the FVR-55 nose cone is shown in Figure 1b. Further details on each
247 instrument are provided below. Comparisons between Cloudy Sky and bench top instruments are presented in Sect.
248 3.

249

250 The Brechtel mSEMS (Model 9404) provided particle number size distributions for diameters between 0.01 to 0.3
251 μm every 30 seconds. Total particle number concentration was obtained by integrating the number concentration
252 over the measured size distribution. The RH of sample air drawn into the mSEMS was $45 \pm 0.74\%$, which was ~
253 40% below ambient RH, for the conditions encountered during flights off the coast of Oregon in August 2022. As
254 for the Clear Sky payload, the MCPC has an $\pm 8\%$ coincidence corrected uncertainty for a particle concentration of
255 $10,000 \text{ cm}^{-3}$.

256

257 A DMT CDP-2 was mounted on the top of a FVR-55 nose cone for measurement of cloud drop number
258 concentration for diameters from 2 to 50 μm and retrieval of liquid water content. Liquid water content was derived
259 from the cloud droplet size distribution provided by the DMT CDP-2. The CDP-2 measures cloud droplet counts

Deleted: 2

Formatted: Line spacing: 1.5 lines

Formatted: Font: 10 pt

Formatted: Font: 10 pt

Formatted: Font: 10 pt

Formatted: Font: 10 pt

and sizes them into 30 bins from 2-30 μm . The count in each bin is converted to a concentration using the cross-sectional surface area of the sensing beam (0.24 m^2) and the speed of the aircraft to determine the volume of air sampled per second. Once the concentration is known, the volume of cloud droplets per volume is calculated and converted to mass per volume assuming density of 1.0.

Table 3. Measured parameters and instrumentation in the Cloudy Sky Payload.

Cloudy Sky Payload Instrumentation			
Measured Parameter	Derivable Parameter(s)	Instrument	Uncertainty
Particle number size distribution and total number concentration (0.01 to 0.3 μm in diameter)	Scattering coefficient, asymmetry parameter, Angstrom exponent ^b	Brechtel miniature Scanning Electrical Mobility Sizer (mSEMS) coupled with a MCPC detector	$\pm 8\%$ ^a
Cloud droplet number concentration and size (2 to 50 μm)	Cloud liquid water content Cloud droplet effective diameter	DMT miniature Cloud Drop Probe (CDP-2)	
T		Rotronic HC2-S3 IST HYT271	$\pm 0.1^\circ\text{C}^{\text{d}}$ (<15 s) ^b $\pm 0.2^\circ\text{C}$ (<15 s) ^b
RH		Rotronic HC2-S3 IST HYT271	$\pm 0.8\%^{\text{d}}$ (<5 s) ^b $\pm 1.8\%$ (<4 s) ^b

^aCoincidence corrected concentration uncertainty at $10,000 \text{ cm}^{-3}$

^bResponse time

3. Comparison of UAS and bench top measurements

The degree of agreement between the bench and payload measurements of particle number concentration and absorption coefficient were evaluated by calculating the relative difference between the measurements as

$$\text{relative difference} = \left(\frac{x_{\text{bench}} - x_{\text{uas}}}{x_{\text{bench}}} \right) \quad (1)$$

where x_{bench} and x_{uas} are the bench and UAS measured values, respectively. The overall experimental uncertainty was calculated as

$$\text{experimental uncertainty} = [(\delta x_{\text{bench}})^2 + [(\delta x_{\text{uas}})^2]^{1/2}] / x_{\text{bench}} \quad (2)$$

where δx_{bench} and δx_{uas} are the uncertainties in the bench and UAS measurements, respectively, as reported in Tables 1 and 2 and taken from manufacturer specifications.

Formatted: Line spacing: 1.5 lines

Deleted: ¶

Deleted: ¶

291 **3.1. Particle number concentration**

292
293 Particle number concentrations measured by the Clear and Cloudy Sky payloads and bench top instruments were
294 compared during ATOMIC (The Atlantic Tradewind Ocean-Atmosphere Mesoscale Interaction Campaign), a cruise
295 in the tropical North Atlantic (Quinn et al., 2021). The comparison took place on January 24, 2020 from 18:40 to
296 22:00 UTC. For both the payload and the bench top instruments, sample air was drawn through a 5 m mast 18
297 m.a.s.l. and forward of the ship's stack. The mast was automatically rotated into the wind to maintain nominally
298 isokinetic flow. Air entered the inlet through a 5-cm diameter hole, passed through a 7° expansion cone, and then
299 into the 20-cm inner diameter sampling mast. The flow through the mast was 1 m³ min⁻¹. The transmission
300 efficiency of the inlet for particles with aerodynamic diameters < 6.5 μm is greater than 95% (Bates et al., 2002).
301 The bottom 1.5 m of the mast was heated so that the sample air was at an RH of 60 ± 5%. Stainless steel tubes
302 extending into the heated portion of the mast were connected to bench top instrumentation and payload inlets with
303 conductive silicone tubing.

304
305 A bench top MAGIC210 particle counter, which measures particles with diameters greater than 0.005 μm, was
306 compared to the Clear Sky MCPC and the Cloudy Sky mSEMS (Figure 3, top of plot). Differential Mobility Particle
307 Sizers (DMPS) and an Aerodynamic Particle Sizer (APS) were used for the comparison to the Clear Sky POPS for
308 particles with diameters greater than 0.14 μm (Figure 3, bottom of plot). A combination of an Aitken DMPS and an
309 Accumulation DMPS measures the size distribution between 0.002 and 0.8 μm in geometric diameter. The APS
310 measures the size distribution between 0.85 and 10.37 μm in aerodynamic diameter. The DMPS and APS size
311 distributions were merged by converting the APS data from aerodynamic to geometric values using calculated
312 densities and associated water mass at 60% RH based on the range of measured chemical compositions reported by
313 Quinn et al. (2002). The DMPSs and APS are housed in a temperature-controlled box at the base of the inlet to
314 maintain a uniform RH across all instruments. Given that the payloads and bench instruments were measured from a
315 common inlet and the residence time in the tubing to the payloads was short, it is likely that RH differences in the
316 sample air delivered to the payload and bench instruments were negligible over the comparison period. The payload
317 data were averaged into 5-minute time periods to match the DMPS/APS scan times.

318
319 The average difference between the bench MAGIC CPC and the Clear Sky payload MCPC number concentration
320 was $22 \pm 42 \text{ cm}^{-3}$, resulting in an average relative difference of $5.2 \pm 0.9\%$. The relative difference is smaller than
321 the overall experimental uncertainty of $9.5 \pm 0.09\%$ indicating good agreement. The coefficient of determination, r^2 ,
322 for the comparison was 0.99. These results indicate that the trends in the two measures of number concentration
323 agreed well. However, the bench instrument was consistently higher by about 5%. Differences could be due to
324 particle losses in sampling lines. Particle losses will be quantified in future experiments.

325
326 The average difference between the bench MAGIC CPC and the Cloudy Sky integrated number concentration from
327 the mSEMS was $-1.9 \pm 9.8 \text{ cm}^{-3}$, resulting in an average relative difference of $-0.19 \pm 0.67\%$. This difference is

Deleted: 5

Deleted: 2

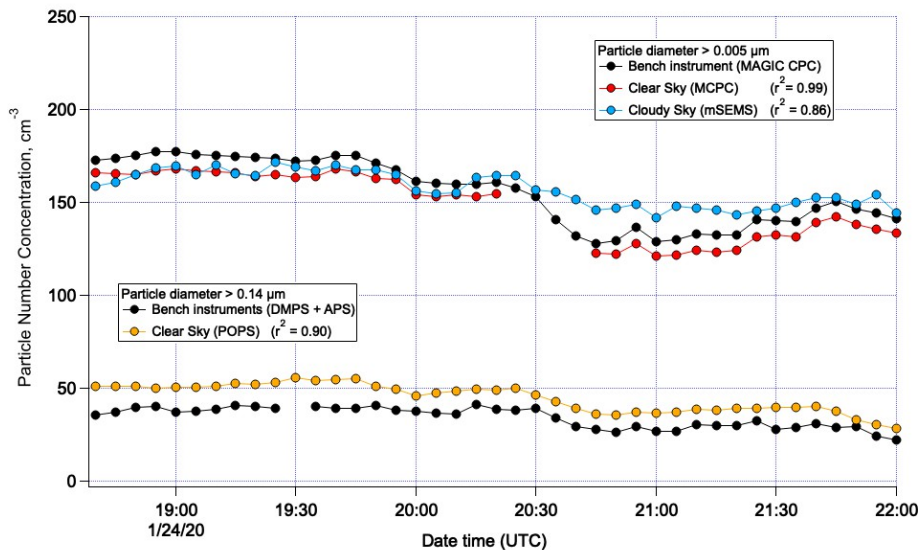
Deleted: 2

Deleted: 86

332 smaller than the overall experimental uncertainty of $10.2 \pm 0.72\%$ indicating good agreement. A correlation between
 333 the two measurements resulted in an r^2 value of 0.86. The mSEMS was, in general lower than the MAGIC CPC for
 334 the first half of the comparison and higher for the second half, most likely due to changes in the mSEMS inversion
 335 routine during the experiment.

336
 337 The average difference between the bench DMPS/APS and the Clear Sky POPS for diameters greater than $0.14 \mu\text{m}$
 338 was $-11 \pm 7.6 \text{ cm}^{-3}$, resulting in an average relative difference of $-31 \pm 6.7\%$. The overall experimental uncertainty
 339 was $13 \pm 0.67\%$ indicating a systemic difference resulting in consistently lower values measured by the DMPS/APS
 340 than the POPS, again likely associated with losses in sampling lines. The r^2 value for the correlation was 0.90.

341
 342 **Figure 3. Comparison of particle number concentrations between bench and payload instruments for diameters**
 343 **greater than $0.005 \mu\text{m}$ (top half of plot) and $0.14 \mu\text{m}$ (bottom half of plot) during ATOMIC on January 24, 2020.**
 344 **Coefficients of determination, r^2 , are for the regression between the payload CN concentration and the bench**
 345 **instrument used for each size range.**



346
 347
 348
 349

3.2. Absorption coefficient

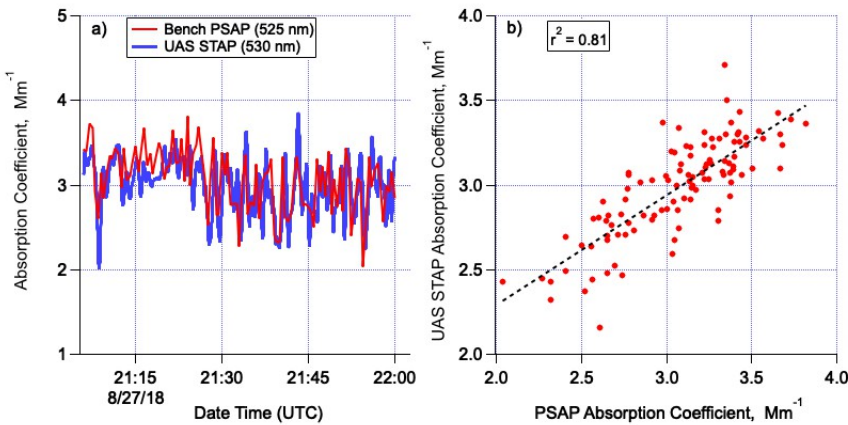
350 The Clear Sky STAP (525 nm) was compared to a Radiance Research PSAP (530 nm) at PMEL on August 27, 2018
 351 from 21:06 to 22:00 UTC. The 5 m mast described above was used to deliver sample air to the bench top PSAP and
 352 to the Clear Sky payload. The bench PSAP was downstream of a Berner multi-jet cascade impactor with a 50%

Deleted:Page Break.....

Deleted: 2

356 aerodynamic cut-off diameter of 1.0 μm and a PermaPure nafion dryer (model PR-94). The Clear Sky STAP also
 357 was downstream of a PermaPure nafion dryer so that both absorption signals were measured at $< 25\%$ RH. Data
 358 were averaged to 30 s to minimize noise. A time series of the comparison and a correlation plot are shown in Figure
 359 4a and b, respectively. The average absolute difference between the bench PSAP and the UAS STAP was $0.11 \pm$
 360 0.34 Mm^{-1} . The average relative difference was $3.1 \pm 12\%$, which was smaller than the overall experimental
 361 uncertainty of $32 \pm 3.9\%$. The r^2 value for the correlation was 0.81.

363 **Figure 4. Comparison of the Bench top PSAP and the Clear Sky UAS STAP as a) a time series and b) a**
 364 **correlation plot. The comparison was done of ambient air at PMEL on 8/27/18.**
 365



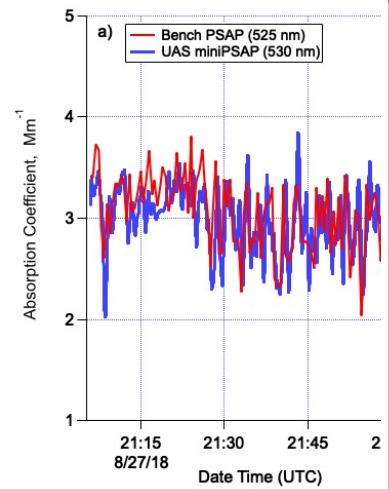
366
 367
 368 **3.3. Aerosol optical depth**

369
 370 Aerosol optical depth (AOD) from the miniSASP was compared to a Solar Light Microtops during Flight 5 over the
 371 Tillamook airport. The lowest altitude flown while the payload was still powered on before landing was 660 m. The
 372 miniSASP measured at 550.4 nm and the Microtops at 500 nm. The miniSASP AODs were adjusted to 500 nm
 373 using the Microtops-measured Ångstrom Exponent. Between 22:45 and 22:50 on August 11, 2022 the Microtops
 374 AOD averaged 0.08 ± 0.01 while the miniSASP measured 0.07 ± 0.02 indicating agreement within overall
 375 uncertainty. The lower average value for the miniSASP could be due to the higher altitude of the measurement. Due
 376 to the limited period of comparison, further tests are warranted.
 377
 378

Deleted: 3

Deleted: Page Break

Deleted: 3



Deleted:

384 **4. Results**

385 **4.1. First shipboard flights**

386 The first shipboard flights of the FVR-55 with payloads onboard took place from March 9 to 11, 2022 from the
387 *TowBoatU.S. Richard L. Becker* off the coast of Key West, FL. A 6 m x 6 m launch pad was installed on the rear
388 deck to minimize interference with boat superstructure during take-off and landing (Figure 5). A total of 11 flights
389 were flown including 2 Functional Check Flights of the UAS, 4 with the Clear Sky payload, and 5 with the Cloudy
390 Sky payload. The first two flights were conducted 25 miles northwest of Key West with the remainder conducted 5
391 miles southeast of Key West. All flights were line-of-sight with a maximum altitude of 360 m due to the Certificate
392 of Authorization (COA) in place. Unfortunately, this low flight ceiling prevented clouds from being sampled. Table
393 4 provides a list of flights with duration, payload configuration, flight pattern, wind speed and ship heave. Wave
394 heights during all flights were observed to be between 0.3 and 0.6 m. Ship speed was 1 to 4 m s⁻¹.

395
396 Three flights occurred on March 10th and March 11th with both payloads being flown. With each payload in its own
397 nose cone, swapping of payloads between flights took 30 to 45 minutes. This time included readying the plane for
398 the next flight (installing fresh batteries and refueling).

399
400 **Figure 5. FVR-55 with the Clear Sky payload onboard on the 6 x 6 m launch pad on the rear deck of the**
401 ***TowBoatU.S. Richard L. Becker.***



402
403
404

Deleted: 4

Deleted: 4

407 **Table 4. Shipboard flight information including duration, payload configuration, flight pattern, wind speed, and**
 408 **ship heave.**

Flight Number	Date	Duration (min)	Payload	Flight Pattern	Wind Speed (m s ⁻¹)	Ship heave (m)
1	3/9/23	21	FCF ^a		7	< 0.3
2 ^b	3/9/23	60	Clear	Spirals between 60 and 335 m		
3	3/9/23	62	Clear	Spirals between 60 and 335 m	5.1	< 0.3
4 ^c	3/10/23	5	Cloudy		4.1	0.3
5	3/10/23	17	FCF ^a		4.6	0.5
6	3/10/23	62	Cloudy	Circles at 335 m	4.9	0.5
7	3/10/23	60	Cloudy	Circles at 335 m	4.6	0.8
8	3/10/23	152	Clear	Circles at 120 and 335 m	2.6	0.3
9	3/11/23	183	Cloudy	Circles at 335 m	6.4	0.9
10	3/11/23	122	Cloudy	Circles at 90, 150, 210, 270, and 335 m	4.9	0.8
11	3/11/23	122	Clear	Racetracks at 150 m	5.6	0.5

409 ^aFunctional Check Flight
 410 ^bTelemetry file corrupted
 411 ^cGenerator failure, flight aborted
 412

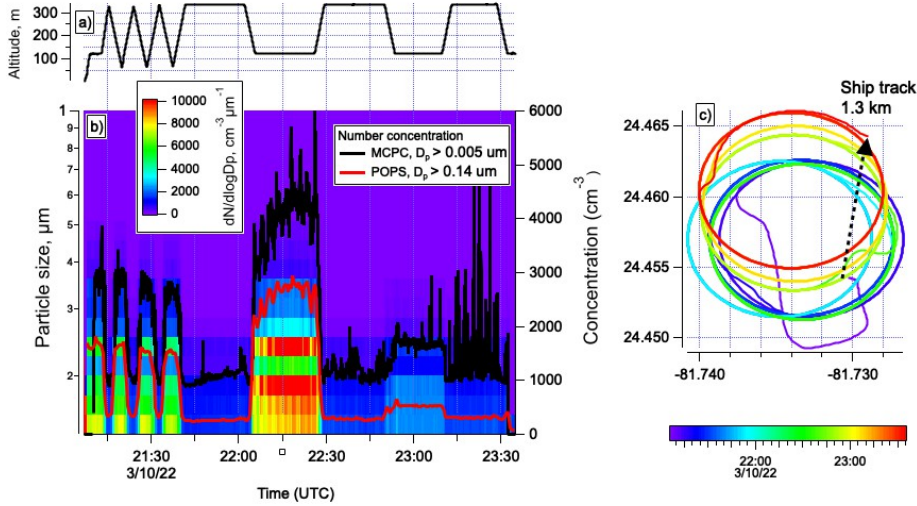
413 Examples of data collected during Clear and Cloudy Sky payload flights are shown in Figures 6 and 7, respectively.
 414 The Clear Sky payload was flown on Flight 8. Initially four vertical profiles between 50 and 335 m were conducted
 415 to identify the altitude of aerosol layers. Circles were then flown alternating between 335 and 120 m (Figure 6a).
 416 Particle number concentrations decreased with height, ranging up to 5,000 cm⁻³ at 120 m and decreasing to 1000 cm⁻³
 417 at 335 m for diameters greater than 0.005 μm (Figure 6b). Concentrations for diameters greater than 0.14 μm were
 418 more than a factor of two lower. This result is expected given the large number concentration at diameters less than
 419 0.2 μm. The flight track colored by time and the ship track are shown in Figure 6c. The ship travelled 1.3 km during
 420 the flight. The plane landed within ± 0.36 m of the programmed spot on the launch pad.

Deleted: 5
 Deleted: 6
 Deleted: 5
 Deleted: 5
 Deleted: 5

421
 422

428 **Figure 6.** Data from the Clear Sky payload during Flight 8 offshore of Key West including a) altitude, b) total
 429 particle number concentration for two size ranges ($D_p > 0.005$ and $0.14 \mu\text{m}$) and particle number size
 430 distribution, and c) the flight track colored by time along with the ship track.
 431

Deleted: 5



432 The Cloudy Sky payload was flown on Flight 6. After the initial ascent, circles were conducted at 335 m, the highest
 433 altitude allowed by the COA in place (Figure 7a). Unfortunately, this altitude was below cloud bottom but the flight
 434 served as a test of the aerosol instrumentation onboard. Initially particle number concentrations were around 3,000
 435 cm^{-3} but increased up to 8,000 cm^{-3} after about 30 minutes of flight time (Figure 7b). As the number concentration
 436 increased, the mean size of the particles shifted from about 0.12 to 0.16 μm . The flight track colored by time and the
 437 ship track during the flight are shown in Figure 7c. The ship travelled 1.3 km during the flight with the plane landing
 438 within ± 0.76 m of the designated spot on the launch pad.
 439
 440
 441
 442

Deleted: 6

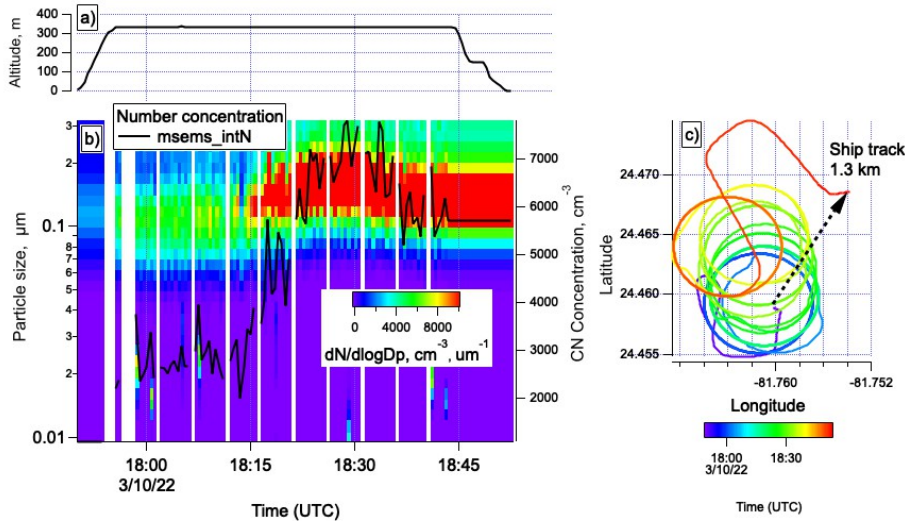
Deleted: 6

Deleted: 6

447 **Figure 7. Data from the Cloudy Sky payload during Flight 6 offshore of Key West including a) altitude, b) total**
 448 **particle number concentration and particle number size distribution, and c) the flight track colored by time along**
 449 **with the ship track.**

Deleted: 6

450
451



452
453
454

4.2. First flights in cloud

455
456 The FVR-55 with payloads onboard was flown from the Tillamook UAS Test Range (TUTR) in cooperation with
 457 the Near Space Corporation (NSC) between August 9th and 17th, 2022. TUTR is located at the Tillamook, OR airport
 458 about 10 km from the coast. Flights were conducted over the airport and in offshore warning areas up to 40 km from
 459 the airport under the NSC COA. Line of sight flights over the airport were conducted up to 1,370 m with the help of
 460 visual observers. For the offshore BVLOS flights, a chase plane escorted the FVR-55 through non-controlled
 461 airspace to the warning areas. NSC personnel communicated flights to the local FAA Air Traffic Control (Seattle
 462 Center) and managed airspace de-confliction. Mission Control was based out of the Tillamook airport control tower.
 463 The science team directed the Pilot-in-Control (PIC) to adjust flight tracks based on incoming, real-time data from
 464 the payloads. Five flights with the Clear Sky payload and 9 flights with the Cloudy Sky payload were conducted for
 465 a total of 38.5 flight hours (see Table 5).

466
467

469 **Table 5. TUTR flight information including duration, payload configuration, and flight pattern. Time within**
 470 **cloud is based on a measured cloud drop number concentration above 5 cm⁻³.**

Flight Number	Date	Duration (min)	Payload	Flight Pattern	Comments
1	8/9/12	120	Cloudy Sky	Tracks below (300 m) and within (470 m) cloud ^a	Over airport
2	8/9/12	123	Cloudy Sky	Tracks below (400 m) and within (530 m) cloud ^a	Over airport
3	8/10/12	118	Cloudy Sky	Tracks below (610 m) and within (760 to 910 m) cloud ^a	Over airport
4	8/10/12	119	Cloudy Sky	Tracks below (610 m) and within (910 to 980 m) cloud ^a	Over airport
5	8/11/22	213	Clear Sky	Chase plane escort to offshore warning area for BVLOS ^b flights. Orbit in aerosol layer at 2550 m.	Offshore up to ~24 NM from airport
6	8/12/22	169	Cloudy Sky	Chase plane escort to offshore warning area for BVLOS ^b flights. Tracks below (800 m), within (1500 m), and above (2000 m) cloud.	Offshore up to ~24 NM from airport
7	8/12/22	168	Cloudy Sky	Tracks below (910 m) and within (1000 m) cloud ^a	Over airport
8	8/13/22	78	Cloudy Sky	Tracks below (1300 m) and within (1370 m) cloud ^a	Over airport
9	8/14/22	151	Clear Sky	Orbit in aerosol layer at 2300 m.	Over airport
10	8/14/22	113	Cloudy Sky	Chase plane escort to offshore warning area for BVLOS ^b flights. Clouds too far away to sample.	Over airport ^c
11	8/15/22	223	Cloudy Sky	Chase plane escort to offshore warning area for BVLOS ^b flights. PIC ^c handoff at Netarts Beach. Tracks below (300 m), within (400 m), and above (490 m) cloud.	Offshore up to ~16 NM from airport
12	8/16/22	152	Clear Sky	Chase plane escort to offshore warning area for BVLOS ^b flights. PIC ^c handoff at Bayocean Beach. Orbit in aerosol layer at 1800 m.	Offshore up to ~16 NM from airport
13	8/16/22				Aborted. Chase plane issue.
14	8/17/22	264	Clear Sky	Orbit in aerosol layer at 1500 m.	Over airport

471 ^aAbove cloud flights were prevented by the line of sight COA over the airport.

472 ^bBeyond visual line of sight

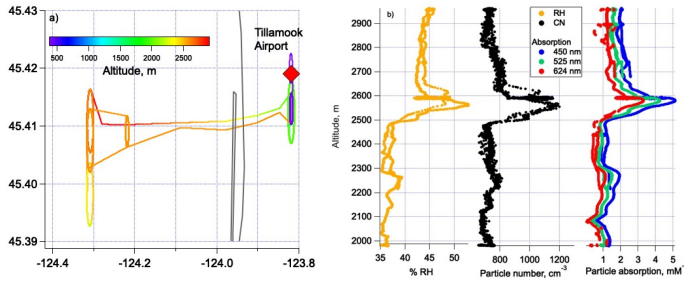
473 ^cPIC = Pilot-In-Control

474
 475 The track from Flight 5 with the Clear Sky payload onboard is shown in Figure 8, along with vertical profiles of RH,
 476 particle number concentration, and aerosol absorption coefficient. The presence of an aerosol layer at ~2550 m is
 477 clear based on increased particle number concentration and aerosol absorption. The factor of 4 increase in absorption
 478 relative to values above and below the layer indicate the aerosol was likely made up of smoke. Results from the
 479 filter sample collected in the aerosol layer show that non-sea salt potassium, a tracer of biomass burning, was
 480 elevated at 0.04 µg m⁻³. HYSPLIT trajectory analysis indicates the sampled air mass was transported northward
 481 along the Oregon coast where several fires were burning according to the NASA FIRMS (Fire Information for

Deleted: 7

483 Resource Management System) web site ([https://firms.modaps.eosdis.nasa.gov/map/#t:adv;d:today;@-](https://firms.modaps.eosdis.nasa.gov/map/#t:adv;d:today;@-117.1,41.0,6.0z)
484 117.1,41.0,6.0z).

485
486 **Figure 8. Flight 5 track from the TUTR colored by altitude (a) and vertical profiles of RH, particle number**
487 **concentration, and absorption coefficient (b).**



Deleted: 7

488
489
490 Vertical profiles of cloud drop number concentration for Flights 4, 6, and 11 are shown in Figure 9. All data points
491 are shown in grey and level leg averaged points are shown in red. Particle number concentrations for diameters
492 between 0.03 and 0.3 μm were derived from the integral of the mSEMS size distribution. A lognormal fit was
493 applied to the size distributions to extend the size range up to 2.0 μm to encompass the entirety of the accumulation
494 mode. The relationship between particle number concentration and cloud drop effective radius for the averaged level
495 leg data from the three flights is shown in Figure 10. Particle number concentration and cloud drop size were well
496 correlated ($r^2 = 0.75$ to 0.97) for all ranges of cloud liquid water contents sampled. An increase in particle number
497 concentration corresponded to a decrease in cloud drop size as expected for the first indirect or Twomey effect
498 (Twomey, 1977). Future data analysis will be done to explore relationships between aerosol number concentration
499 and size, cloud drop number concentration and size, and liquid water content for clouds at different altitudes.

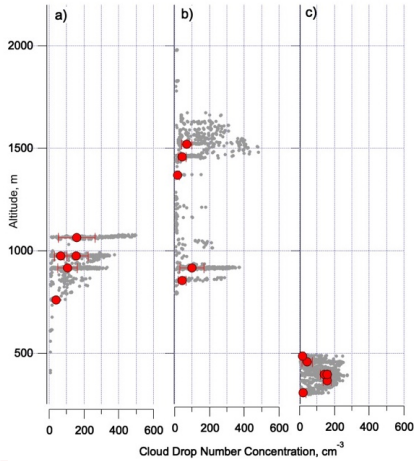
Deleted: 8

Deleted: 9

500
501

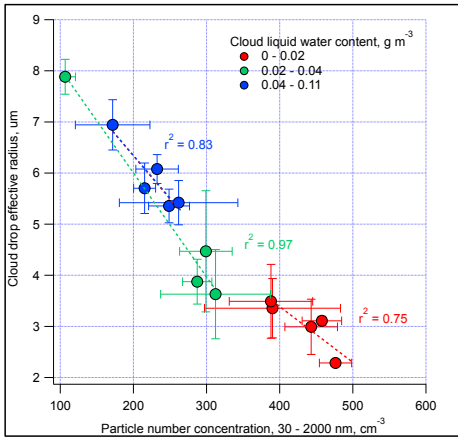
505
506

Figure 9. Vertical profiles of cloud drop number concentration for Flights a) 4, b) 6, and c) 11 from the TUTR. All data points are shown in grey and level leg averaged points are shown in red.



507
508
509
510
511
512
513
514

Figure 10. Comparison of particle number concentration for diameters between 0.03 and 2.0 μm and cloud drop effective radius averaged over the altitude level leg data shown in Figure 8. Data are binned by ranges of cloud liquid water content.



515
516
517

Deleted:Page Break.....

Deleted: 8

Deleted: ¶

Deleted: 9

523 **5.0. Conclusions**

524

525 The initial results described here indicate that the FVR-55 UAS with Clear and Cloudy Sky payloads onboard offers
526 a unique platform for observations relevant to aerosol direct and indirect radiative forcing. This observing platform
527 is deployable at sea with less cost and greater flight frequency than a crewed air craft. Potential applications of this
528 technology extend beyond aerosol – cloud observations to marine mammal assessments, harmful algal blooms, and
529 radiative impacts from forest fires.

530

531 Next steps include upgrading to the larger L3Harris Fixed Wing VTOL Rotator, the FVR-90. The Clear and Cloudy
532 Sky payloads will be integrated into FVR-90 nose cones which will allow for the addition of instruments and longer
533 flight endurance. The planned added instruments include upward and downward looking pyranometers to assess
534 direct connections between particle number and concentration, cloud drop concentration and size, and radiation. In
535 addition, instrumentation will be added to both payloads for the measurement of particle number size distributions
536 from 5 nm to 3 μm . Although larger, the FVR-90 is operable from a ship thereby fulfilling the need of aerosol,
537 cloud, and radiation measurements in the marine atmosphere.

538

539 **Data availability**

540 Flight data are publicly available at <https://saga.pmel.noaa.gov/Field/Tillamook2022/>.

541

542 **Author contributions**

543

544 PKQ and TSB designed the experiments. DJC and JEJ built and operated the payloads. LMU analyzed the chemical
545 data. PKQ prepared the manuscript with contributions from all co-authors.

546

547 The authors declare that they have no conflict of interest.

548

549 **Acknowledgements**

550 We thank Aaron Farber and the entire L3Harris Latitude Engineering team for developing, fabricating, and flying
551 the FVR-55. We thank the captain and crew of the TowBoatUS Richard L. Becker and Chuck Bagnato and Eric
552 Waters from the Tillamook UAS Test Range for their contributions toward successful flights. We thank Alexander
553 Smirnov of NASA GSFC for the microtops calibration, processing, and data quality assurance. We also thank
554 NOAA OMAO and UxSRTO for logistical and financial support. This is PMEL contribution number 5537.

555

556 **References**

557

558 Anderson, T. L., Covert, D. S., Wheeler, J. D., Harris, J. M., Perry, K. D., Trost, B. E., Jaffe, D. J., and Ogren, J.:
559 Aerosol backscatter fraction and single scattering albedo: Measured values and uncertainties at a coastal station in
560 the Pacific Northwest, *Journal of Geophysical Research - Atmospheres*, 104, 26,793 - 726,807, 1999.

561 Aurell, J., Mitchell, W., Chirayath, V., Jonsson, J., Tabor, D., and Gullett, B.: Field determination of multipollutant,
562 open area combustion source emission factors with a hexacopter unmanned aerial vehicle, *Atmospheric*
563 *Environment*, 166, 433 - 440, 2017.

564 Bates, T. S., Coffman, D. J., Covert, D. S., and Quinn, P. K.: Regional marine boundary layer aerosol size
565 distributions in the Indian, Atlantic and Pacific Oceans: A comparison of INDOEX measurements with ACE-1 and
566 ACE-2, and Aerosols99, *Journal of Geophysical Research - Atmospheres*, 107, 8026, 2002.

567 Bates, T. S., Quinn, P. K., Johnson, J. E., Corless, A., Brechtel, F. J., Stalin, S. E., Meinig, C., and Burkhardt, J. F.:
568 Measurements of atmospheric aerosol vertical distributions above Svalbard, Norway, using unmanned aerial systems
569 (UAS), *Atmospheric Measurement Techniques*, 6, 2115 - 2120, 2013.

570 Bond, T. C., Anderson, T. L., and Campbell, D.: Calibration and intercomparison of filter-based measurements of
571 visible light absorption by aerosols, *Aerosol Science and Technology*, 30, 582 - 600, 1999.

572 Brady, J. M., Stokes, M. D., Bonnardel, J., and Bertram, T. H.: Characterization of a Quadrotor Unmanned Aircraft
573 System for Aerosol-Particle-Concentration Measurements, *Environmental Science and Technology*, 50, 1376 - 1383,
574 2016.

575 Chilinski, M. T., Markowicz, K. M., and Markowicz, J.: Observation of vertical variability of black carbon
576 concentration in lower troposphere on campaigns in Poland, *Atmospheric Environment*, 137, 155 - 170, 2016.

577 Corrigan, C. E., Roberts, G. C., Ramana, M. V., Kim, D., and Ramanathan, V.: Capturing vertical profiles of aerosols
578 and black carbon over the Indian Ocean using autonomous unmanned aerial vehicles, *Atmospheric Chemistry and*
579 *Physics*, 8, 737 - 747, 2008.

580 Gao, R. S., Telg, H., McLaughlin, R., Ciciora, S. J., Watts, L., Richardson, M. S., Schwarz, J. P., Perring, A. E., T.D.,
581 T., Rollins, A. W., Markovic, M. Z., Bates, T. S., Johnson, J. E., and Fahey, D. W.: A Light-Weight, High-Sensitivity
582 Particle Spectrometer for PM_{2.5} Aerosol Measurements, *Aerosol Science and Technology*, 50, 88 - 99, 2016.

583 Haywood, J. and Ramaswamy, V.: Global sensitivity studies of the direct radiative forcing due to anthropogenic
584 sulfate and black carbon aerosols, *Journal of Geophysical Research - Atmospheres*, 103, 6043 - 6058, 1998.

585 IPCC: *Climate Change 2021: The Physical Science Basis* Cambridge University Press 2021.

586 Li, J., Carlson, B. E., Yung, Y. L., Lv, D., Hansen, J., Penner, J., Liao, H., Ramaswamy, V., Kahn, R., Zhang, P.,
587 Dubovik, O., Ding, A., Lacis, A. A., Zhang, L., and Dong, Y.: Scattering and absorbing aerosols in the climate
588 system, *Nature Reviews Earth and Environment*, 3, 363 - 379, 2022.

589 Lohmann, U. and Feichter, J.: Global indirect aerosol effects: a review, *Atmospheric Chemistry and Physics*, 5, 715 -
590 737, 2005.

591 Murphy, D. M., Telg, H., Eck, T. F., Rodriguez, J., Stalin, S. E., and Bates, T. S.: A miniature scanning sun
592 photometer for vertical profiles and mobile platforms, *Aerosol Science and Technology*, 50, DOI:
593 10/1080/027/86826.2015.1121200, 2016.

594 Quinn, P. K., Coffman, D. J., Bates, T. S., Miller, T. L., Johnson, J. E., Welton, E. J., Neusüß, C., Miller, M., and
595 Sheridan, P. J.: Aerosol optical properties during INDOEX 1999: Means, variability, and controlling factors, *Journal*
596 *of Geophysical Research - Atmospheres*, 10.1029/2000JD000037, 2002.

597 Quinn, P. K., Thompson, E. J., Coffman, D. J., Baidar, S., Bariteau, L., Bates, T. S., Bigorre, S., Brewer, A., de Boer,
598 G., de Szoeké, S. P., Drushka, K., Foltz, G. R., Intrieri, J., Iyer, S., Fairall, C. W., Gaston, C. J., Jansen, F., Johnson,
599 J. E., Kruger, O. O., Marchbanks, R. D., Moran, K. P., Noone, D., Pezoa, S., Pincus, R., Plueddemann, A. J.,
600 Pohlker, M. L., Poschl, U., Quinones Melendez, E., Royer, H. M., Szczodrak, M., Thomson, J., Upchurch, L. M.,
601 Zhang, C., Zhang, D., and Zuidema, P.: Measurements from the RV Ronald H. Brown and related platforms as part
602 of the Atlantic Tradewind Ocean-Atmosphere Mesoscale Interaction Campaign (ATOMIC), *Earth System Science*
603 *Data*, 13, 1759 - 1790, 2021.

604 Rosenfeld, D., Zhu, Y., Wang, M., Zheng, Y., Goren, T., and Yu, S.: Aerosol-driven droplet concentrations dominate
605 coverage and water of low-level clouds, *Science*, 363, 10.1126/science.aav0566, 2019.

606 Russell, P. B., Hobbs, P. V., and Stowe, L. L.: Aerosol properties and radiative effects in the United States East Coast
607 haze plume: An overview of the Tropospheric Aerosol Radiative Forcing Observational Experiment (TARFOX),
608 *Journal of Geophysical Research - Atmosphere*, 104, 2213 - 2222, 1999.

609 Takemura, T., Nakajima, T., Dubovik, O., Holben, B. N., and Kinne, S.: Single-scattering albedo and radiative
610 forcing of various aerosol species with a global three-dimensional model, *Journal of Climate*, 15, 333 - 352, 2002.

611 Telg, H., Murphy, D. M., Bates, T. S., Johnson, J. E., Quinn, P. K., Giardi, F., and Gao, R. S.: A practical set of
612 miniaturized instruments for vertical profiling of aerosol physical properties, *Aerosol Science and Technology*, 51,
613 715 - 723, 2017.

614 Twomey, S.: The influence of pollution on the shortwave albedo of clouds, *Journal of Atmospheric Science*, 34,
615 1149 - 1152, 1977.

616 Yoon, S.-C. and Kim, J.: Influences of relative humidity on aerosol optical properties and aerosol radiative forcing
617 during ACE-Asia, *Atmospheric Environment*, 40, 4328 - 4338, 2006.

618 Zhang, Y., Forrister, H., Liu, J., Dibb, J., Anderson, B., Schwarz, J., Perring, A. E., Jimenez, J., Campuzano-Jost, P.,
619 Wang, Y., Nenes, A., and Weber, R. J.: Top-of-atmosphere radiative forcing affected by brown carbon in the upper
620 troposphere, *Nature Geoscience*, 10, 486 - 489, 2017.

621